11th AIAA/CEAS Aeroacoustics Conference, May 23–25, 2005, Monterey, California

Effects of Inflow Conditions and Subgrid Model on LES for Turbulent Jets

Niklas Andersson* , Lars-Erik Eriksson† and Lars Davidson†

Division of Fluid Dynamics, Department of Applied Mechanics, Chalmers University of Technology, SE-412 96 Göteborg, Sweden

The turbulent mixing process prescribing the spreading rate of the jet and the length of the potential core region is influenced by a number of factors. Using large-eddy simulation (LES), the four factors that are believed to be the most important in this respect are: subgrid-scale properties, the accuracy of the numerical scheme, the entrainment boundary conditions, and the inflow conditions. In a previously performed study of a subsonic (Mach 0.75) jet, the turbulence mixing was found to be too efficient and hence the length of the potential core region was underpredicted. In that study indications were found of that the overpredicted mixing was due to the inflow conditions. For a model nozzle, capturing the initial turbulent shear flow might not be of that great importance for accurate prediction of radiated sound since most of these effects will appear in the high-frequency range. When dealing with real engine geometries, however, it becomes quite important. Moreover, methods for industrial use have to cope with complex geometries and high temperature and velocity ratios making the ability to capture the initial flow physics even more important.

In the present work LES has been used for the same Mach 0.75 jet. The acoustic field is extracted to the far field using Kirchhoff surface integration. The effects of inflow conditions, Reynolds number, and subgrid-scale model on flowfield and acoustic signature are investigated.

The Favre-filtered Navier-Stokes equations were solved using a finite-volume method solver with a low-dissipation third-order upwind scheme for the convective fluxes, a second-order centered difference approach for the viscous fluxes and a three-stage second-order Runge-Kutta technique in time. The computational domain was discretized using a block-structured boundary-fitted mesh with approximately 3.0×10^6 cells. The calculations were performed on a parallel computer, using message-passing interface (MPI). A compressible form of Smagorinsky's subgrid-scale model was used to compute the subgrid-scale stresses. Absorbing boundary conditions based on characteristic variables were adopted for all free boundaries.

*Ph.D. Student, Division of Fluid Dynamics, Department of Applied Mechanics, Chalmers University of Technology, SE-412 96 Göteborg, Sweden

†Professor, Division of Fluid Dynamics, Department of Applied Mechanics, Chalmers University of Technology, SE-412 96 Göteborg, Sweden

Copyright © 2005 by Niklas Andersson, Lars-Erik Eriksson & Lars Davidson. Published by the American Institute of Aeronautics and Astronautics, Inc. with permission.

Nomenclature

Latin symbols

c	speed of sound
$\mathcal{C}_{ij}$	Cross stress
C_p	specific heat at constant pressure
$C_R,\ C_I$	Smagorinsky model coefficients
e	energy
k	kinetic energy
$\mathcal{L}_{ij}$	Leonard stress
p	pressure
Pr	Prandtl number
Q	state vector
q_j	energy diffusion vector
r	radial coordinate or distance from source to observer
$\mathcal{R}_{ij}$	Reynolds stress
Re_D	Reynolds number based on the jet diameter
$\mathcal{S}$	cell face area
S_{ij}	strain rate tensor
T	temperature
t	time
u_i	Cartesian components of velocity vector
$\mathbf{x}$	flowfield location
x_i	Cartesian coordinate vector component
$\mathbf{y}$	far-field location

Greek symbols

Δ	filter width
δ_{ij}	Kronecker delta
γ	gas constant
μ	dynamic viscosity
ρ	density
σ_{ij}	viscous stress tensor
τ_{ij}	subgrid-scale stress tensor
τ_r	retarded time
ε	turbulence dissipation rate

Subscripts

0	total condition
∞	freestream or ambient conditions
j	jet, nozzle-exit condition
rms	root-mean-square
t	turbulent quantity

Superscripts

$''$	unresolved fluctuation
$-$	spatially filtered quantity
$'$	resolved fluctuation
$\sim$	spatially Favre-filtered quantity
$\wedge$	Fourier transform

SGS	subgrid scale

Symbols

$\langle \dots \rangle_\theta$	circumferentially averaged quantity
$\langle \dots \rangle_t$	time-averaged quantity

I. Introduction

THE number of commercial aircraft in service is continuously growing and airports around the world are growing in size, which increases exposure to air traffic noise in populated areas. Threshold values for noise certification of new aircraft are based on global restrictions on noise generated by air traffic. Moreover, local restrictions for air ports with heavy traffic limit operating hours or even impose direct noise penalty costs. Stricter regulations on noise levels in the surroundings of airports have made the abatement of near-ground operation noise an important issue for aircraft and engine manufacturers, and noise generation has now become an important design factor that is taken into consideration early in the construction process.

Using a grid fine enough in the far-field regions to minimize the introduction of sound propagation errors, the acoustic field can be obtained directly from the flowfield simulation. This requires a detailed numerical compressible flow simulation, e.g. direct numerical simulation (DNS), see for example Freund[1] and Mitchell *et al.*,[2] or large-eddy simulation (LES), as in e.g. Bogey *et al.*[3,4,5,6] and Mankbadi *et al.*[7] In DNS, all scales of the turbulent flowfield are computed accurately, which requires a mesh fine enough to capture even the smallest scales of the flow, whereas in LES only the large scales of the flow are resolved and the influence on these large scales of the smaller, unresolved scales is modeled using a subgrid-scale model. With the computational resources available today, DNS is restricted to fairly simple geometries and low Reynolds number flows. Moreover, it is believed, see Mankbadi,[8] that large scales are more efficient than small ones in generating sound, which justifies the use of LES for sound predictions. To save computational time, a hybrid approach may be used in which the computational problem is divided into two parts. An LES can be used to obtain the unsteady non-linear near field, which in the jet noise case corresponds to the hydrodynamic jet region. The acoustic field is then extended to far-field observer locations using, for example, Kirchhoff[9] surface integration, see Lyrintzis[10] and Freund *et al.*[11] Using a hybrid approach may even lead to noise predictions of higher quality than a direct approach since the amount of numerical dissipation to which the sound waves are exposed is decreased. Furthermore, the frequency cut-off is often higher in the integration surface regions than in the far field.[12,13]

Andersson *et al.*[14,15,16] used LES to study the flow and radiated sound of a subsonic (Mach 0.75) jet at different heating conditions. In these studies the initial turbulence mixing was found to be too efficient, which resulted in underprediction of the potential core lengths. The predicted acoustic signature was in generally good agreement with experimental data though. For the forward arc observers the sound pressure levels (SPL) were, however, somewhat overpredicted, which is believed to be due to high-frequency noise generated in the initial jet region as a consequence of the overpredicted turbulent mixing.

The reason for the underprediction of the length of the potential core region can probably be found in a combination of several factors. At the time when the present study was initiated the factors believed to be the most important were: subgrid-scale viscosity; numerical scheme and resolution; entrainment boundary conditions and inflow conditions. DeBonis *et al.*[17] reported an underprediction of the potential core region when using LES for the simulation of a supersonic jet. It was discussed in that work that the reason for the underprediction was a lack of subgrid dissipation. Furthermore, it has been mentioned by Morris *et al.*[18] that changes in the subgrid-scale model constants affect the potential core length and the initial growth of the jet. DeBonis[19] found that the potential core region could be extended by increasing the subgrid-scale dissipation. This might seem to be a quite natu-

ral effect since the increased subgrid-scale viscosity decreases the intensity of the resolved turbulent fluctuations and hence the shear-layer mixing becomes less efficient and that this in turn leads to an elongated region of potential flow. However, as will be shown in the present study, this is not always the case. Although the correct potential core length might be obtained by modification of the subgrid-scale properties alone, a more physical approach would be to modify the inflow conditions to produce results in better agreement with measurements. The shape of the velocity profile and turbulence level at the nozzle exit might be factors that are important for the development of the jet. Thin boundary layers at the nozzle exit results in steep velocity gradients in the initial part of the shear layer and thus a more violent encounter with the irrotational surrounding fluid. This may result in larger fluctuations and thus also higher degree of turbulent mixing. Bogey *et al.*[5] investigated the effects of the inflow conditions on the jet flow. It was found that the use of a thinner shear-layer momentum thickness resulted in higher turbulence intensities in the shear-layer and hence a more rapid transition. In the present study the effect of specifying a velocity profile at the nozzle inlet and that of adding synthesized turbulence at the inlet boundary has been investigated.

Tucker[20] used a scheme for the convective fluxes based on a weighted average of centered and upwind biased components. It was found that even with a weak blending of fifth-order upwinding with a fourth order central scheme, i.e. only small contributions from the upwind biased components, the effects of the upwind scheme is still evident. However, the effect of the artificial dissipation introduced by the numerical scheme ought to be the same as that of the subgrid-scale dissipation, i.e. more numerical dissipation should lead a delayed shear layer transition. Consequently, the numerical scheme used in Refs. 14–16 does probably not introduce too much artificial dissipation since the turbulent mixing is overpredicted. Concerning the effects of the entrainment flow, only the correct mass flow will give the correct flow behavior in the hydrodynamic region. A lack of entrained mass will be compensated by a back flow, which results in a recirculation zone surrounding the jet preventing it from spreading correctly.

The present work has been conducted within the EU 5th framework program JEAN[a] which was an European project investigating the physics behind noise generation in single-stream jets. In the continuation of this project, CoJeN[b], the flowfield and radiated sound of a high-subsonic coaxial nozzle/jet configuration is being investigated. The objective of CoJeN is to develop and validate prediction tools that can be used by the aerospace industry to assess and optimize jet noise prediction techniques. The aim is to provide design tools that can be used to develop low-noise nozzles for high bypass ratio (HBR) engines. For prediction techniques to be useful to industry, the methods must cope with realistic jet flows such as coaxial jet configurations with high velocities, significant velocity and temperature gradients, and arbitrary nozzle geometries. Hence, the ability to capture the initial flow physics becomes even more important.

II. Overview of the Present Study

The effects of changes in inflow conditions, Reynolds number, and subgrid-scale model on the flow in the initial jet region and on the radiated sound of an isothermal Mach 0.75 jet have been investigated. The results are validated against near-field and far-field measurements obtained by Jordan *et al.*[21,22,23] These measurements have also been reported in part by Power *et al.*[24] A simulation of a corresponding jet previously reported by Andersson *et al.*[14,15,16] is used as a reference. This reference simulation is referred to as *Jet I*. In the present study the results of six simulations, *Jet II – Jet VII*, of the single-stream jet will be reported. Table 1 gives more detail on these simulations in terms of modifications made from the *Jet I* simulation. In the reference simulation the Reynolds number was decreased from approximately 9.0×10^5, which was the Reynolds number in the measurements, to 5.0×10^4 by

[a]JEAN – Jet Exhaust Aerodynamics & Noise, Contract number: G4RD-CT-2000-000313

[b]CoJeN – Computation of Coaxial Jet Noise, contract number: AST3-CT-2003-502790.

modifying the viscosity on the assumption that the flow is only weakly Reynolds number dependent. To justify this assumption, a simulation was made (*Jet II*) with the Reynolds number for which the measurements were obtained. For this simulation wall functions were used near the nozzle walls. Obviously, this is a rather coarse LES since no changes were made to the mesh and this is a fact that should be considered when analyzing the results of this simulation. The Reynolds number in *Jet III* to *Jet VII* is the same as in the reference simulation. In *Jet III*, the inlet conditions have been modified by adding synthesized turbulent velocity fluctuations. In *Jet IV*, the numerical accuracy has been improved by adding a flux correction term that approximates the effect of the Leonard stresses that appears in the spatially filtered Navier-Stokes equations. This flux correction technique will be described in more detail in Section IV-C. *Jet V – Jet VI* are both simulations where the subgrid-scale dissipation has been modified by changing the filter width. In *Jet VII*, a profile for total pressure has been specified at the nozzle inlet boundary so as to generate thicker boundary layer at the nozzle exit and thus change the shear layer behavior in the initial part of the jet.

Table 1. Jet flow simulations

Jet I	Reference simulation $U_j/c_\infty = 0.75$, $Re^*_D = 5.0 \times 10^4$, $T_j/T_\infty = 1.0$
Jet II	Reynolds number corresponding to the experimental Reynolds number $Re_D = 9.0 \times 10^5$ (wall functions are used near the nozzle walls)
Jet III	Synthesized inlet turbulence based on random Fourier modes[25]
Jet IV	Introduction of a Leonard flux correction technique that approximates the effect of the Leonard stresses ($\mathcal{L}_{ij} = \widetilde{\tilde{u}_i\tilde{u}_j} - \tilde{u}_i\tilde{u}_j$)
Jet V	Increased subgrid-scale viscosity by increasing the filter width in the subgrid-scale model ($\Delta = \sqrt{2}(\Delta_1\Delta_2\Delta_2)^{1/3}$)
Jet VI	Decreased subgrid-scale viscosity by decreasing the filter width in the subgrid-scale model ($\Delta = \min(\Delta_1, \Delta_2, \Delta_3)$)
Jet VII	Specified inlet profile ($P_0 = P_0(r)$)

* The Reynolds number was decreased using modified viscosity

A. Aerodynamic and Acoustic Measurements Used for Validation

The measurements were made within the JEAN project by Jordan *et al.*[21,22,23] at the MARTEL facility of CEAT (Centre d'Etudes Aeródynamiques et Thermiques), Poitiers, France. Two-component single-point and mono-component two-point measurements were made using Laser Doppler Velocimetry (LDV). The acoustic field was sampled using an arc of microphones at 30 jet diameters and 50 jet diameters from the jet exit, respectively. For greater detail on the experimental set-up see Jordan *et al.*[21,22] and Jordan & Gervais.[23]

III. Governing equations

The equations solved are the spatially Favre-filtered continuity, momentum and energy equations,

$$\frac{\partial \overline{\rho}}{\partial t} + \frac{\partial(\overline{\rho}\tilde{u}_i)}{\partial x_i} = 0 \tag{1}$$

$$\frac{\partial(\overline{\rho}\tilde{u}_i)}{\partial t} + \frac{\partial(\overline{\rho}\tilde{u}_i\tilde{u}_j)}{\partial x_j} = -\frac{\partial \overline{p}}{\partial x_i} + \frac{\partial \overline{\sigma}_{ij}}{\partial x_j} + \frac{\partial \tau_{ij}}{\partial x_j} \tag{2}$$

$$\begin{aligned} &\frac{\partial\left(\overline{\rho}\tilde{e}_0\right)}{\partial t} + \frac{\partial\left(\overline{\rho}\tilde{e}_0\tilde{u}_j\right)}{\partial x_j} = -\frac{\partial \overline{p}\tilde{u}_j}{\partial x_j} + \\ &+ \frac{\partial}{\partial x_j}\left(C_p\frac{\mu}{Pr}\frac{\partial \tilde{T}}{\partial x_j} + q_j\right) + \frac{\partial}{\partial x_j}\left(\tilde{u}_i\left(\overline{\sigma}_{ij} + \tau_{ij}\right)\right) \end{aligned} \tag{3}$$

where $\overline{\sigma}_{ij}$ and τ_{ij} are the Favre-filtered viscous stress tensor and subgrid-scale viscous stress tensor, respectively. These are here defined as

$$\overline{\sigma}_{ij} = \mu\left(2\tilde{S}_{ij} - \frac{2}{3}\tilde{S}_{mm}\delta_{ij}\right) \tag{4}$$

$$\tau_{ij} = \mu_t\left(2\tilde{S}_{ij} - \frac{2}{3}\tilde{S}_{mm}\delta_{ij}\right) - \frac{2}{3}\overline{\rho}k^{SGS}\delta_{ij} \tag{5}$$

where k^{SGS} is the subgrid-scale kinetic energy

$$k^{SGS} = C_I\Delta^2\tilde{S}_{mn}\tilde{S}_{mn} \tag{6}$$

μ_t the subgrid-scale dynamic viscosity

$$\mu_t = C_R\overline{\rho}\Delta^2\sqrt{\tilde{S}_{mn}\tilde{S}_{mn}} \tag{7}$$

and $\tilde{S}_{ij}$ is the Favre-filtered strain rate tensor given by,

$$\tilde{S}_{ij} = \frac{1}{2}\left(\frac{\partial\tilde{u}_i}{\partial x_j} + \frac{\partial\tilde{u}_j}{\partial x_i}\right) \tag{8}$$

The subgrid heat flux appearing in the Favre-filtered energy equation is modeled using a temperature gradient approach

$$q_j = C_p\frac{\mu_t}{Pr_t}\frac{\partial\tilde{T}}{\partial x_j} \tag{9}$$

The filter-width in Eqs. (6) and (7) is the local grid cell width, i.e. $\Delta = \left(\Delta_1\Delta_2\Delta_3\right)^{1/3}$. It should be noted that this quantity was changed in the *Jet IV* and *Jet V* simulations. The subgrid-scale model used in this work is the Smagorinsky part of the model proposed by Erlebacher *et al.*[26] for compressible flows. Constants C_R and C_I that appear in Eqs. (6) and (7) are the Smagorinsky model constants, of which the latter is a constant in the compressibility correction term. The constants are here given by

$$\left\{\begin{array}{rcl} C_R &=& 0.012 \\ C_I &=& 0.0066 \end{array}\right. \tag{10}$$

The system of governing equations, Eqs. (1–3), is closed by making assumptions on the thermodynamics of the gas considered. It is assumed that the gas is thermally perfect, i.e. it obeys the gas law. Furthermore, the gas is assumed to be calorically perfect, which implies that internal energy and enthalpy are linear functions of temperature.

IV. Method

A. Numerical Scheme

The Favre-filtered Navier-Stokes equations were solved using a finite volume method solver with a third-order low-dissipation upwind scheme for the convective fluxes and a centered difference approach for the diffusive fluxes. The temporal derivatives were estimated using a second-order three-stage Runge-Kutta technique. The solver used is based on the G3D family of codes developed by Eriksson.[27] The convective scheme is a combination of centered and upwind biased components that have been used with good results for free shear flows by Mårtenson *et al.*[28] and, more recently, for shock/shear-layer interaction by Wollblad *et al.*[29] The coefficients of low-dissipation upwind scheme for estimation of the convective flux over a cell face are derived using a third-order polynomial $Q(x)$ to represent the variation of the flow state in the direction normal to the face as

$$Q(x) = A + Bx + Cx^2 + Dx^3 \tag{11}$$

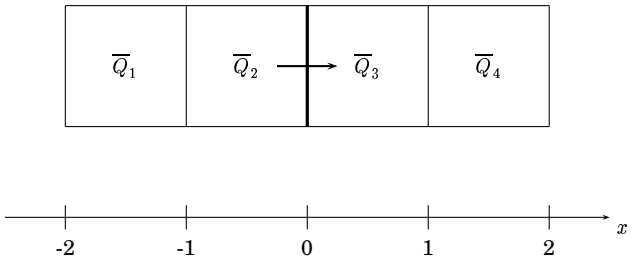

Figure 1. The face state, Q_0, is estimated using the state in four neighboring cells.

The face state is evaluated using the interpolated value $Q(0)$, modified to include upwinding by adding the third derivative of $Q(x)$ according to

$$\begin{aligned} Q_0 &= Q(0) + \delta Q'''(0) = A + 6\delta D = \\ &= C_1\overline{Q}_1 + C_2\overline{Q}_2 + C_3\overline{Q}_3 + C_4\overline{Q}_4 \end{aligned} \tag{12}$$

where coefficient δ in front of the upwind term has been chosen by numerical experiments[28] to be $(1/96)$ in order to introduce only a small amount of upwinding and thus ensure as high numerical accuracy as possible. The result is the low-dissipation third-order upwind scheme with the coefficients

$$\begin{cases} C_1 = -\left(\frac{1}{12} + \delta\right) = -\frac{9}{96} \\ C_2 = \left(\frac{7}{12} + 3\delta\right) = \frac{59}{96} \\ C_3 = \left(\frac{7}{12} - 3\delta\right) = \frac{53}{96} \\ C_4 = -\left(\frac{1}{12} - \delta\right) = -\frac{7}{96} \end{cases} \tag{13}$$

For more detail on the numerical scheme, see Eriksson[27] or Andersson.[16]

B. Synthesized Inlet Turbulence

In the *Jet III* simulation, synthesized turbulence was added at the nozzle inlet in the form of fluctuating velocity components. In each solver time step new turbulence velocity components for locations at the nozzle inlet plane are generated using a turbulence synthesize method based on random Fourier modes

and levels of turbulence kinetic energy, k, and turbulence dissipation rate, ε, specified for the nozzle inlet. A short description of the synthesize methodology will be given in this section. Greater detail on the method is given in the PhD thesis by Billson[25] or in Billson *et al.*[30,31,32]

For each location, velocity components v_i are generated as a sum of 30 Fourier modes as

$$\mathbf{v}(\mathbf{x}) = 2\sum_{n=1}^{30} \hat{u}_n \cos(\mathbf{k}_n \cdot \mathbf{x} + \psi_n)\sigma_n \tag{14}$$

where $\hat{u}_n$, ψ_n and σ_n are, respectively, the amplitude, phase and direction of the n^{th} Fourier mode. The direction is defined by three angles in wave-space: φ_n, α_n and θ_n. These angles and the phase, ψ_n, are chosen randomly for each Fourier mode. The direction σ_n is a vector with length 1.0. The amplitude of each mode $\hat{u}_n$ is computed from a model turbulence energy spectrum function, $E(k_n)$, corresponding to the energy spectrum of isotropic turbulence as

$$\hat{u}_n = \sqrt{E(k_n)\Delta k_n} \tag{15}$$

where Δk_n is a small interval in the spectrum located at k_n. The parameters in the model spectrum are obtained from the values of k and ε specified at the boundary. In this way the sum of $\hat{u}_n^2$ over all n equals the specified turbulence kinetic energy. The inlet boundary values of k and ε were obtained assuming a 5% turbulence intensity and a turbulence length scale corresponding to $0.2D_{nozzle}$.

The velocity fluctuations, u_i, added to the inlet mean velocity are obtained from the synthesized fluctuations, v_i, as

$$u_i^m = au_i^{m-1} + b(v_i^m + v_i^{m-1}) \tag{16}$$

where m denotes time step and a and b define a low-pass filtering of the synthesized velocity components and are here defined as $a = \exp^{-\Delta t/\tau}$ and $b = \sqrt{(1.0-a)/2}$, respectively. The time scale, τ, that appears in the denominator of the exponent in the expression for a corresponds to convection of frozen turbulence and is defined as $\tau = l_t/U_c$ where l_t is a turbulence length scale and U_c is a convection velocity representative for the nozzle inlet plane. The use of a low-pass filter makes the effective number of Fourier modes represented greater than the 30 modes used in each turbulence realization.

C. Leonard Flux Correction Implementation

In the *Jet IV* simulation, a flux correction term that approximates the effects of the Leonard stresses has been implemented. The Leonard stresses appears when the convective terms in the momentum and energy equations are filtered spatially. A spatial Favre filter is used in this work, i.e. a mass weighted spatial filter, leading to governing equations on the form given by Eqs. 2–3. Favre filtering is a common filtering approach for compressible flows since it results in governing equations in a convenient form. Moreover, using a filter approach in which fluctuations in density are considered would lead to more complicated subgrid-scale terms. With such a filter, subgrid-scale terms would appear in the continuity equation, terms that would need modeling of their own.[33] Using Favre filtering, the flow properties are decomposed as follows

$$\Phi = \tilde{\Phi} + \Phi^{''} \tag{17}$$

where $\tilde{\Phi}$ is a Favre-filtered, resolved quantity and $\Phi^{''}$ is the unresolved part of Φ. The Favre-filtered part of Φ is obtained as follows

$$\tilde{\Phi} = \frac{\overline{\rho\Phi}}{\overline{\rho}} \tag{18}$$

in contrast to Favre time averaging

$$\tilde{\Phi} \neq \tilde{\bar{\Phi}} \tag{19}$$

and hence

$$\widetilde{\Phi''} \neq 0 \tag{20}$$

Applying the Favre filtering procedure to the convective term in the momentum equation gives

$$\begin{aligned}\overline{\frac{\partial \rho u_i u_j}{\partial x_j}} &= \frac{\partial}{\partial x_j}\left(\overline{\rho\left(\tilde{u}_i + u_i''\right)\left(u_j + u_j''\right)}\right) = \frac{\partial}{\partial x_j}\left(\overline{\rho\tilde{u}_i\tilde{u}_j} + \overline{\rho\tilde{u}_i u_j''} + \overline{\rho u_i''\tilde{u}_j} + \overline{\rho u_i'' u_j''}\right) = \\ &= \frac{\partial}{\partial x_j}\left(\overline{\rho}\tilde{u}_i\tilde{u}_j + \underbrace{\overline{\rho}\widetilde{\tilde{u}_i\tilde{u}_j} - \overline{\rho}\tilde{u}_i\tilde{u}_j}_{\mathcal{L}_{ij}} + \underbrace{\overline{\rho}\widetilde{\tilde{u}_i u_j''} + \overline{\rho}\widetilde{u_i''\tilde{u}_j}}_{\mathcal{C}_{ij}} + \underbrace{\overline{\rho}\widetilde{u_i'' u_j''}}_{\mathcal{R}_{ij}}\right)\end{aligned} \tag{21}$$

Analogous for the convective term in the energy equation

$$\begin{aligned}\overline{\frac{\partial \rho e_0 u_j}{\partial x_j}} &= \frac{\partial}{\partial x_j}\left(\overline{\rho\left(\tilde{e}_0 + e_0''\right)\left(u_j + u_j''\right)}\right) = \frac{\partial}{\partial x_j}\left(\overline{\rho\tilde{e}_0\tilde{u}_j} + \overline{\rho\tilde{e}_0 u_j''} + \overline{\rho e_0''\tilde{u}_j} + \overline{\rho e_0'' u_j''}\right) = \\ &= \frac{\partial}{\partial x_j}\left(\overline{\rho}\tilde{e}_0\tilde{u}_j + \underbrace{\overline{\rho}\widetilde{\tilde{e}_0\tilde{u}_j} - \overline{\rho}\tilde{e}_0\tilde{u}_j}_{\mathcal{L}_{ij}} + \underbrace{\overline{\rho}\widetilde{\tilde{e}_0 u_j''} + \overline{\rho}\widetilde{e_0''\tilde{u}_j}}_{\mathcal{C}_{ij}} + \underbrace{\overline{\rho}\widetilde{e_0'' u_j''}}_{\mathcal{R}_{ij}}\right)\end{aligned} \tag{22}$$

The terms denoted $\mathcal{L}_{ij}$, $\mathcal{C}_{ij}$, and $\mathcal{R}_{ij}$ in Eqs. 21–22 are often referred to as the Leonard stress, cross term, and Reynolds subgrid-scale stress, respectively. In the present work the Leonard stresses have not been evaluated explicitly. Instead a flux correction term has been introduced, later referred to as the Leonard flux correction term. The effect of the flux correction operation corresponds to the effect of the Leonard stress $\mathcal{L}_{ij}$ in the filtered equations. The reason for using this technique is that the finite-volume method used is considered to be tightly coupled to the LES filter. The filtered equations are not solved for explicitly, rather the numerical method acts as a box filter, which gives the filtered flowfield as a result.

The Leonard stresses as given in Eqs. 21–22 are not Galilean invariant, they are therefor often rewritten by combining the Leonard stress and the cross term on the form $\mathcal{L}_{ij} = \widetilde{\tilde{u}_i\tilde{u}_j} - \tilde{\tilde{u}}_i\tilde{\tilde{u}}_j$, which is Galilean invariant.[34] However, since the numerical scheme is not Galilean invariant in itself, it is not believed to be of that great importance for this work to implement the stresses in the Galilean invariant formulation.

When evaluating the convective fluxes in the solver version without the flux correction technique implemented, the first terms on the right hand sides of Eqs. 21–22 are obtained using face averages of $\overline{\rho}$, $\tilde{u}_i$ and $\tilde{e}_0$. These face averages are obtained using the third-order upwind scheme described in Section IV-A. The Reynolds stress terms are approximated using the subgrid-scale model defined by Eqs. 5–7.

An approximation of the variation of the state vector on primitive form, i.e. $q = (\rho, u_i, p)$, over a cell face is be obtained as

$$q = q^A + \frac{\partial q}{\partial J}J + \frac{\partial q}{\partial K}K \tag{23}$$

where q^A is a cell face average obtained as the average of the two adjacent cells on each side of the cell face and $\frac{\partial q}{\partial J}$ and $\frac{\partial q}{\partial K}$ are, respectively, the derivatives of the state vector with respect to J and K, which are the two directions in computational space aligned with the cell face plane, see Figure (2). These derivatives are obtained as

$$\begin{aligned}\frac{\partial q}{\partial J} &= \frac{1}{2}\left(\tilde{q}_{i,j+1,k} - \tilde{q}_{i,j-1,k} + \tilde{q}_{i+1,j+1,k} - \tilde{q}_{i+1,j-1,k}\right) \\ \frac{\partial q}{\partial K} &= \frac{1}{2}\left(\tilde{q}_{i,j,k+1} - \tilde{q}_{i,j,k-1} + \tilde{q}_{i+1,j,k+1} - \tilde{q}_{i+1,j,k-1}\right)\end{aligned} \tag{24}$$

Using Eq. 23 to estimate the state vector values in Gauss points depicted in Figure (2), the Leonard

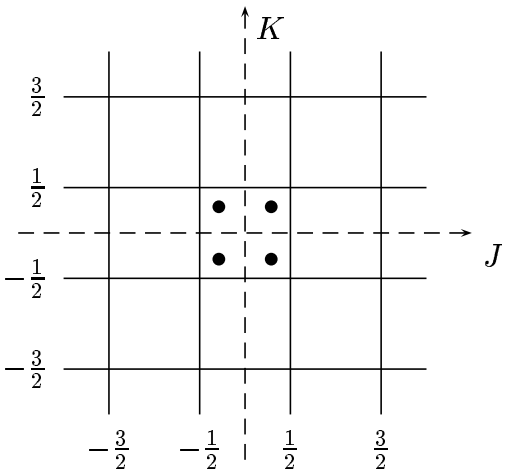

Figure 2. Leonard stresses are evaluated using integration based on Gauss points. The Gauss points are located at $\left(J = \pm\frac{1}{\sqrt{12}}, K = \pm\frac{1}{\sqrt{12}}\right)$ and are indicated by black dots in the figure.

flux correction can be obtained as the difference between the integral based on Gauss points and the integral of face averages over the cell face according to

$$\begin{aligned} \mathcal{L}eonard\ Flux\ Correction &= \int\int_{face} \rho q_p u_q n_q \, d\mathcal{S} - \rho^A q_p^A u_q^A n_q \mathcal{S} \\ &\simeq \sum_{G=1}^{4} \rho^G q_p^G u_q^G n_q^G \Delta\mathcal{S} - \rho^A q_p^A u_q^A n_q \mathcal{S} \end{aligned} \tag{25}$$

where $\mathcal{S}$ and G denote cell face area and Gauss point, respectively.

D. Kirchhoff Surface Integral Formulation

Kirchhoff integration is a method for predicting the value of a property Φ governed by the wave equation, at a point outside a surface enclosing all generating structures.[10] The method was originally used in the theory of diffraction of light and in other problems of an electromagnetic nature[9] but has recently been extensively used for aeroacoustic applications. The integral relation is given by

$$\Phi(\mathbf{y}, t) = \frac{1}{4\pi} \int_S \left[\frac{\Phi}{r^2} \frac{\partial r}{\partial n} - \frac{1}{r} \frac{\partial \Phi}{\partial n} + \frac{1}{c_\infty r} \frac{\partial r}{\partial n} \frac{\partial \Phi}{\partial t} \right]_{\tau_r} dS(\mathbf{x}) \tag{26}$$

where $\mathbf{y}$ is a observer location in the far field and $\mathbf{x}$ a location on the surface. τ_r denotes that the expression within brackets is to be evaluated at retarded time, i.e. emission time. τ_r is related to the observer evaluation time, t, by the distance from the surface to the observer, $r = |\mathbf{y} - \mathbf{x}|$, and the speed of sound in the far-field region, c_∞, as

$$\tau_r = t - \frac{r}{c_\infty} \tag{27}$$

The variable Φ that is to be evaluated in this case is the surface pressure. S denotes the surface enclosing all sound generating structures and n denotes the direction normal to the surface. Surface

S must be placed in a region where the flow is completely governed by a homogeneous linear wave equation with constant coefficients.[11] Greater detail on the Kirchhoff surface integration method is given in e.g. Freund *et al.*[11] and Lyrintzis.[10]

E. Computational Set-up

Figure (3) gives an schematic overview of the computational domain used for the LES reported in this paper. In this figure, the upper half of the three-dimensional domain is shown. In order to minimize the effect of reflections at the domain outlet on the predicted flowfield, a damping zone was added at the domain outlet. The functionality of this damping zone or buffer layer is described in more detail in Andersson *et al.*[14] and Andersson.[15] The axial extent of the physical part of the domain downstream of the nozzle exit is 2.5 meters, which is equal to 50 nozzle diameters ($D_j = 50\ mm$). The radial extent is 10 D_j at the nozzle-exit plane and 20 D_j at the domain outlet. The physical part of the computational domain was discretized using a block-structured boundary-fitted mesh with 33 mesh blocks and approximately 3×10^6 cells. Additionally 5×10^5 cells were used to discretize the damping zone. In order to avoid a center line singularity and to establish mesh homogeneity through out the domain, a combination of polar and Cartesian blocks was used. The grid cells are stretched in the downstream direction and radially towards the boundaries. The mesh has been described in more detail in Refs. 14–16. The nozzle geometry included in the calculation domain corresponds to the last contraction of the nozzle configuration in the experimental set-up.

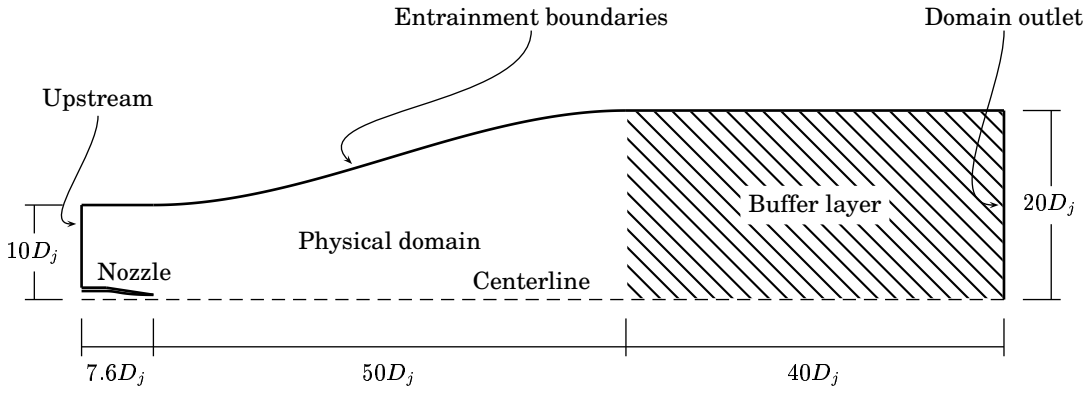

Figure 3. Computational set-up

For all free boundaries, i.e. the upstream and entrainment boundaries, absorbing boundary conditions based on the method of characteristics were adopted. Static pressure was specified at the domain outlet, i.e. at the downstream end of the buffer layer, and at the nozzle inlet P_0 and h_0 were specified. Constant values of these quantities were used in all simulation except in *Jet VII* where the total pressure was specified as an inlet profile $P_0 = P_0(r)$. In the *Jet III* simulation, synthesized turbulence fluctuations were added to the nozzle inlet velocity. The generation of these turbulence velocity components were described in more detail in Section IV-B. The velocities specified at the entrainment boundaries were interpolated from a corresponding RANS calculation. The calculation domain used for the RANS computation is sufficiently large to ensure that no disturbances caused by the outlet boundaries will reach the location of the LES domain boundaries. Figure (4) shows a comparison of the LES and RANS calculation domains.

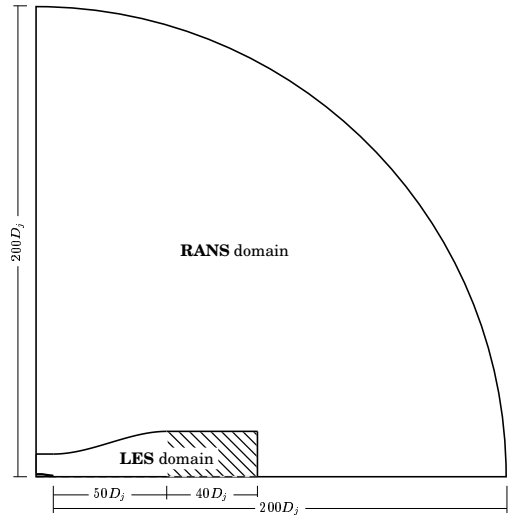

Figure 4. Entrainment velocities were obtained from RANS calculations performed using a significantly larger domain.

V. Results

A. Initial Jet Development

This section compares the results for the simulations mentioned in the introductory part of the paper, see Table (1). Comparisons of the simulations are made in terms of differences in shear layer development, flow statistics in the near-nozzle region and acoustic signature. The results of the simulations referred to as *Jet II – Jet VII* are compared to corresponding quantities obtained for the reference simulation, *Jet I*. For validation of the predicted flow quantities, measured data obtained for the same nozzle geometry and flow conditions have been included in the comparison of time-averaged flow quantities, far-field sound pressure levels and power spectra of far-field pressure.

1. Instantaneous Flowfield

Figure (5) shows entropy contours, $s = P/\rho^{\gamma}$, in the near-nozzle region for the reference case, *Jet I*, and in Figure (6) corresponding contours for *Jet II – Jet VII* are shown. Compared with the contours obtained for *Jet I*, the simulations in which the filter width has been modified are those that differs the most. Increasing the filter width leads, naturally since the subgrid-scale dissipation increases, to less structures in the initial part of the shear layer whereas decreasing the filter width gives a more rapid transition process and thicker shear layer close to the nozzle outlet, see Figures (6(d))–(6(e)). In *Jet II*, where the Reynolds number simulated is higher than in the reference simulation as well as in the other simulations reported in this work, structures appearing upstream of the nozzle exit close to the nozzle walls are much more prominent than in the other cases. These structures are, however, not fully trusted to be correctly represented since, as mentioned in the paper introduction, the mesh is the same as in the simulations with lower Reynolds number. The contours obtained for *Jet III*, *Jet IV* and *Jet VII* are similar to those obtained for *Jet I*.

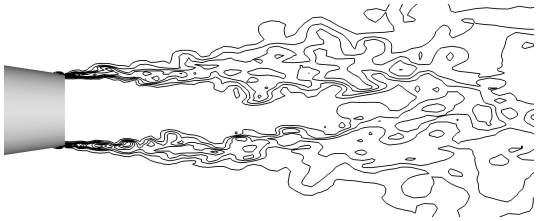

Figure 5. Entropy contours in the near-nozzle regions for the reference case (*Jet I*)

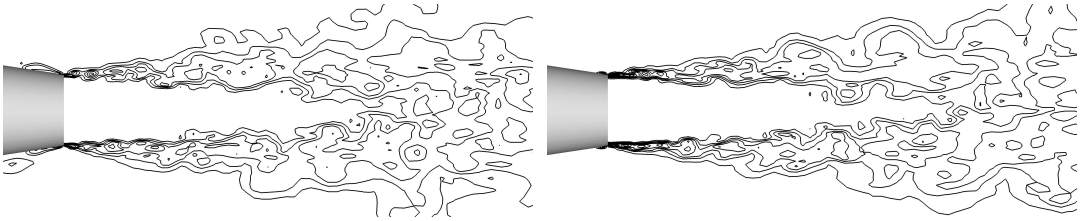

(a) *Jet II* ($Re_D = 9.0 \times 10^5$)

(b) *Jet III* ($Synthesized\ inlet\ turbulence$)

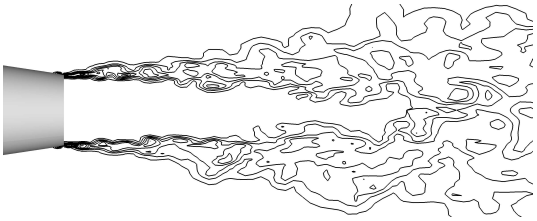

(c) *Jet IV* ($\mathcal{L}eonard\ flux\ correction$)

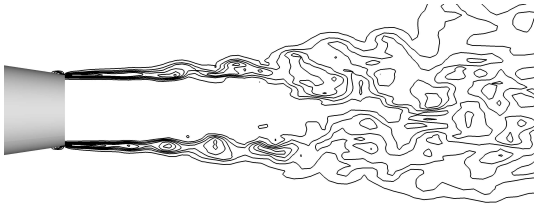

(d) *Jet V* ($\Delta = \sqrt{2}(\Delta_1\Delta_2\Delta_3)^{1/3}$)

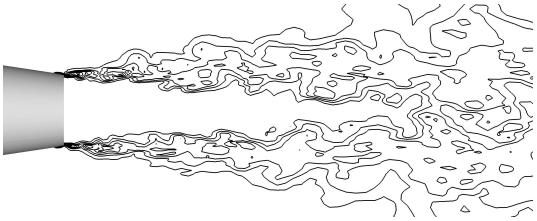

(e) *Jet VI* ($\Delta = \min(\Delta_1, \Delta_2, \Delta_3)$)

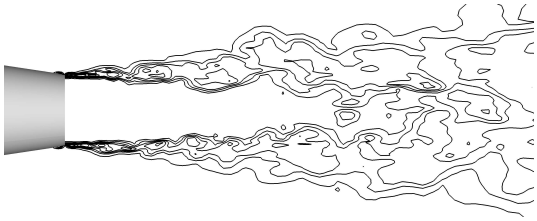

(f) *Jet VII* ($P_0 = P_0(r)$)

Figure 6. Entropy contours in the near-nozzle region for *Jet I – Jet VI*

2. Time-averaged Flowfield

In this section profiles of time-averaged quantities obtained in the initial jet region are compared for the different jet simulations. The predicted data are compared to measured data. Figure (7) shows locations of lines along which axial and radial profiles of time-averaged flow quantities have been

extracted. Note that for the radial profiles, flow quantities have been averaged both in time and in the azimuthal direction so as to improve the statistical convergence. Figures (8–11) show comparisons of

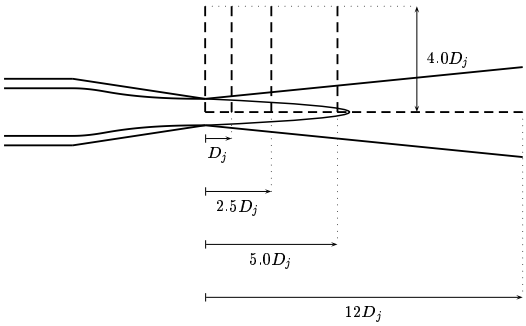

Figure 7. Profiles of axial velocity and second-order moments were obtained along the centerline and along four radial lines.

profiles of time-averaged flow data for *Jet I – Jet VII*. Note that the radial profiles have been staggered corresponding to the downstream location and that the turbulence intensities and $u'v'$-correlations for these profiles have been multiplied by factors 8 and 140, respectively.

As can be seen from the Figures, there are only small differences in flow statistics in the initial flow region for most simulations made. The length of the predicted potential core is insignificantly changed from the reference simulation except for in the simulation with increased filter width (*Jet V*), in which the potential core is somewhat shorter, see Figure (8(a)). The decay rate of centerline axial velocity is also different for *Jet V*. Figure (9) shows a comparison of radial profiles of the $u'v'$ correlation, which is an indication of the degree of mixing in the jet. Again only small differences are observed for all simulations except for *Jet V*. For the profile extracted at $x/D_j = 1.0$, the $u'v'$ correlation obtained from *Jet V* is insignificantly larger than zero. For the subsequent locations, however, the levels in *Jet V* are higher than in the other simulations. This result is consistent with the observed shorter potential core in this case. The reason for this behavior is that the increased filter width results in a delay of the shear layer transition process as mentioned in the previous section. This in turn leads to that the transition process, once initiated, becomes more violent, which leads to higher levels of turbulence kinetic energy and a higher degree of mixing. The higher levels of turbulence kinetic energy in *Jet V* are also indicated by the increase in u_{rms} and v_{rms} seen in Figures (10) and (11), respectively. The predicted peaks in the centerline profiles of turbulence intensities obtained for *Jet V* are shifted towards the nozzle exit, see Figures (10(a)) and (11(a)). This is consistent with the fact that the potential core is shorter in this case since the location of maximum turbulence intensity coincides approximately with the location where the potential core ends. It should be noted, however, that the levels of turbulence intensities for *Jet V* are close to the peaks of the rms-values obtained for the measured data. However, turbulence intensities obtained in the measurements are significantly higher close to the nozzle exit than in the simulations, which might affect the maximum turbulence levels obtained. Some minor differences can be identified for the other simulations. *Jet II* and *Jet VI* gives slightly higher values of u_{rms} and $u'v'$ than most of the other simulations, which can be seen in the radial profiles depicted in Figures (10(b)) and (9). The centerline turbulence intensities are not fully converged, which makes the profiles uneven for axial locations downstream of the potential core region. Thus any conclusions drawn from differences observed in this region are rather uncertain. With this in mind it is noted that for *Jet VI*, the values of v_{rms} along the centerline is somewhat lower for axial locations downstream of $x/D_j = 4$. This is the simulation for which the subgrid-scale dissipation was decreased. Also, the levels of v_{rms} are higher for *Jet III* close to the nozzle exit. However, in this case one would expect even higher levels since synthesized turbulence has been added at the nozzle inlet.

This gives an indication of that a mesh refinement inside the nozzle might be required in order to avoid these fluctuations to be too affected by numerical dissipation.

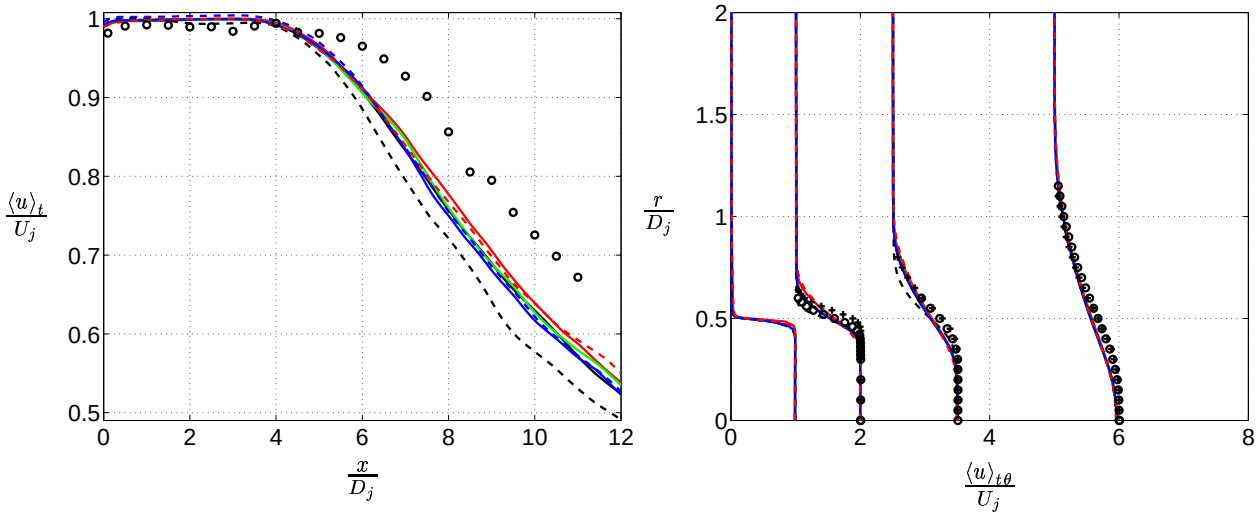

(a) Axial profiles at centerline

(b) Radial profiles

Figure 8. Profiles of axial velocity. Solid black lines denote *Jet I*; solid red lines denote *Jet II*; solid blue lines denote *Jet III*; solid green lines denote *Jet IV*; dashed black lines denote *Jet V*; dashed red lines denote *Jet VI* and dashed blue lines denote *Jet VII*. Black circles and pluses denote measured data[21,24] obtained for the same nozzle geometry and flow conditions as the predictions.

B. Far-field Acoustic Signature

This section gives a presentation of sound pressure levels and power spectra of pressure signals for a few observer locations in the far field. The pressure signals were obtained using Kirchhoff surface integration. The observer locations coincide with the microphone locations in the experimental set-up,[22] see figure (12). More detail on the method can be found in Refs. (14, 16).

Figure (13) depicts entropy contours in the jet region and dilatation contours further away from the jet for the *Jet I* simulation. In Figure (14) corresponding contour plots obtained for *Jet II – Jet VII* are depicted. As can be seen in all these figures, the sound waves radiated in the sideline direction are dissipated rather effectively. This is due to the fact that the mesh is not fine enough in that region to support the acoustic waves in the radial direction. This effect has been discussed in some detail in previously published work where the same computational set-up was used, see Refs. (14, 16). Comparing the dilatation contours obtained for *Jet I* with those obtained for *Jet II – Jet VII*, the most noticeable differences are found for *Jet V*, see Figure (14(d)). In this case the intensity of the high-frequency content in the sound radiated to the forward arc seems to be augmented. Moreover, the sound radiated to the rear arc is significantly changed. The introduction of the Leonard flux correction seems to improve the quality of the predicted radiated sound, see Figure (14(c)).

To further evaluate differences in the predicted acoustic signature, sound pressure levels and spectra of far-field pressure signals were obtained. The results are validated against available measured data provided by Laboratoire d'Etude Aeródynamiques. The results for *Jet I* have previously been

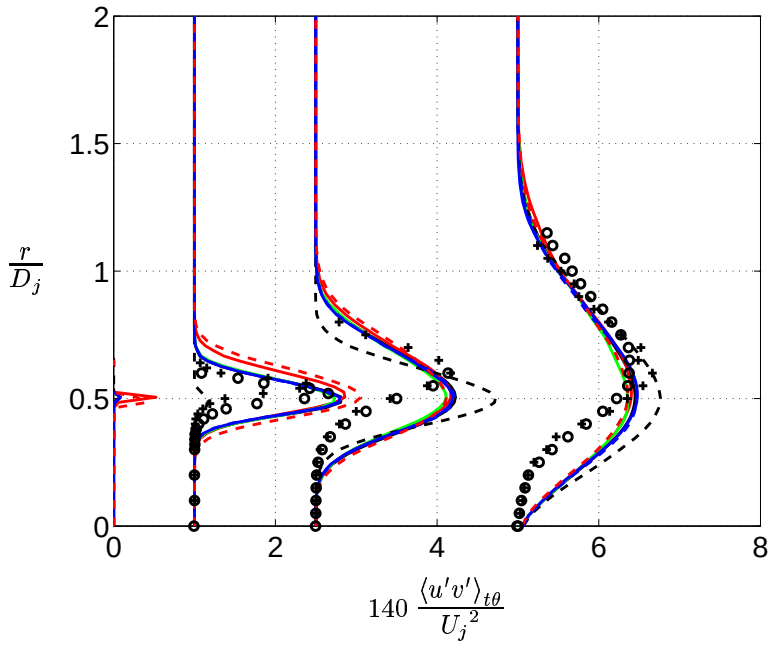

Figure 9. Radial profiles of $u'v'$. See also legend to Figure (8).

reported in Refs. (14, 16). Figures (15) through (20) give comparisons of predicted spectra and sound pressure levels. As can be seen in Figure (17(a)), the predicted spectra are better aligned with spectra obtained from measured data for *Jet IV* than for *Jet I*. Especially noticeable is that overprediction of high frequencies for $140°$ observer is decreased for *Jet IV*. It seems that introducing the Leonard flux correction technique improves the representation of the higher frequency content of the radiated sound and that this results in sound pressure levels in better agreement with measured levels for the forward arc observers, see Figure (17(b)). It should be noted, however, that for *Jet IV*, the sound pressure levels for the intermediate angles, i.e. the observers most affected by numerical dissipation, is even more underpredicted than for the reference simulation. The sound pressure levels obtained for *Jet V* are for all observers higher than in the reference simulation, see Figure (18(b)). The reason for this increase in SPL can be found in increased spectrum amplitudes. As can be seen in Figure (18(a)), the low frequency range amplitudes of the spectra are higher than those obtained for *Jet I* for all observers represented. As mentioned in the previous paragraph, this effect was also indicated in the dilatation contours for *Jet V* , see Figure (14(d)). The *Jet VI* simulation gives SPL somewhat lower for the rear arc observers than the reference simulation, see Figure (19(b)). *Jet II*, *Jet III* and *Jet VII* gives predicted sound pressure levels and spectra comparable to those of *Jet I*, see Figures (15), (16) and (20).

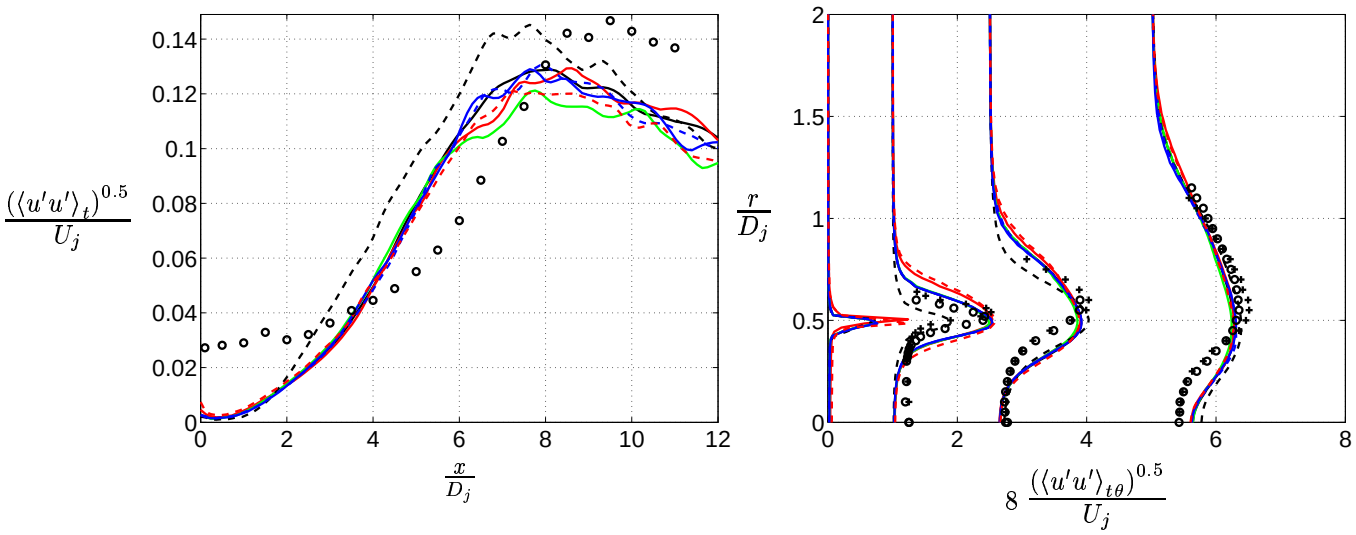

(a) Axial profiles at centerline

(b) Radial profiles

Figure 10. Profiles of u'_{rms}. See also legend to Figure (8).

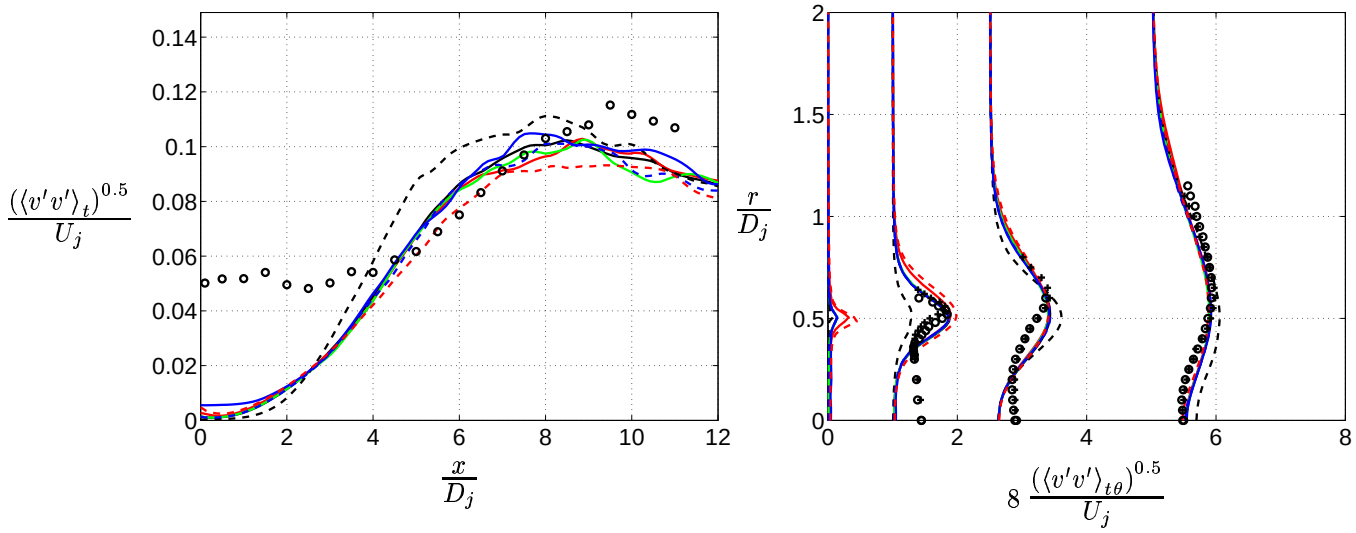

(a) Axial profiles at centerline

(b) Radial profiles

Figure 11. Profiles of v'_{rms}. See also legend to Figure (8).

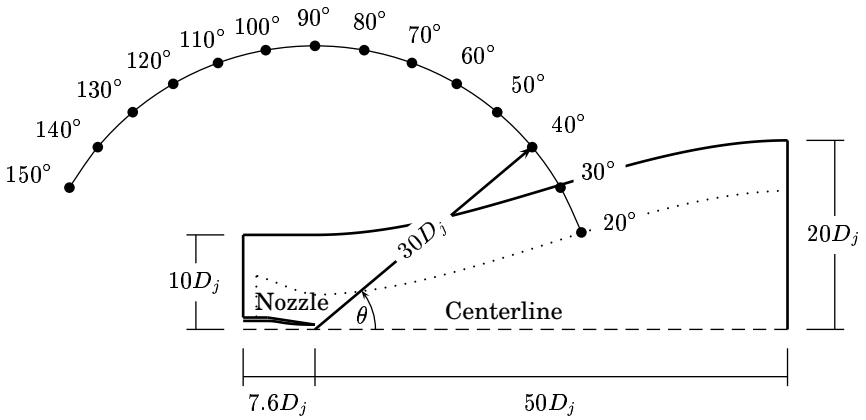

Figure 12. Acoustic pressure fluctuations were evaluated in 14 observer locations situated on an arc in the far-field region of the jet. The arc has its center at the nozzle-exit plane. The dotted line denotes the Kirchhoff surface used.

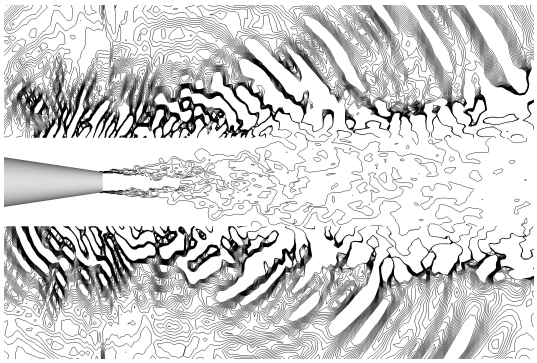

Figure 13. Entropy and dilatation contours for the reference case (*Jet I*)

VI. Concluding Remarks

In the present work, large-eddy simulation has been used for the simulation of a single-stream nozzle/jet configuration. The sensitivity of the flow in the near-nozzle region and the radiated sound to changes in subgrid-scale quantities, inflow conditions and Reynolds number have been investigated. The results have been compared to previously published results for the single-stream jet[14,16] and measurements[21,22,23] obtained for the same geometry and flow conditions. Short descriptions of the simulations for which results are reported in this paper are listed below.

Jet I	reference simulation[14,16]
Jet II	The simulated Reynolds number corresponds to the Reynolds number. for which the measurements were obtained
Jet III	synthesized inlet turbulence
Jet IV	Leonard flux correction
Jet V	increased filter width
Jet VI	decreased filter width
Jet VII	specified inlet profile

Only the simulation with increased filter width gave significant changes in the near-nozzle flow statistics. The increased subgrid-scale dissipation results in a lower degree of mixing close to the nozzle than for the other simulations presented. This in turn leads to a more violent mixing process once initiated, which can be seen in the higher levels of resolved turbulence intensities and overpredicted $u'v'$ correlation for this jet. The potential core is somewhat shorter in this simulation than in the others, which is consistent with the higher degree of mixing. Moreover, the rate of decay of the centerline axial velocity is slightly increased for this jet. None of the changes from the reference simulation gave a potential core length in better agreement with the measured data. It was discussed by Sagaut[35] that, although LES might be able to capture the physics of shear layer flows, quantities such as the potential core length in the jet case are almost never captured. In summary, it seems that, although some changes to the shear layer flow can be observed in the simulations made in this work, the flow statistics in the near-nozzle region is rather insensitive to changes in inflow parameters and subgrid-scale quantities.

A rough comparison of the predicted acoustic signatures was made by comparing contours of dilatation in the far field. Compared to the reference simulation, increasing the subgrid-scale filter width results in augmented high-frequency content of the forward radiated sound as well as significant changes to the sound radiated to the rear arc. The introduction of the Leonard flux correction terms seems to improve the quality of the predicted acoustic signature. The other simulations gives dilatation contours comparable to those obtained for the reference case.

Sound pressure levels in the far field were evaluated with a hybrid approach. Kirchhoff surface integration was utilized for the propagation of sound to locations in the far field. Introducing flux correction terms that approximate the effects of the Leonard stresses appearing in the spatially filtered governing equations gave a better representation of the high-frequency content of the radiated sound. Observer locations situated on the forward arc are affected to a higher degree than the rear arc observers by high-frequency noise generated in the shear layer region. Thus the improved representation of the higher frequency content results in sound pressure levels that are better aligned with the measured levels for the upstream observers. It should be mentioned, however, that this improvement comes with a penalty in terms of calculation cost. The iteration wall time when the Leonard flux correction was implemented in the solver was roughly 4/3 times the iteration time for the other simulations.

VII. Acknowledgment

This work was conducted in part within the EU 5th Framework Project JEAN (Jet Exhaust Aerodynamics & Noise), contract number: G4RD-CT-2000-000313 and in part within the EU 6th Framework Project CoJeN (Computation of Coaxial Jet Noise), contract number: AST3-CT-2003-502790.

References

[1]Freund, J., "Noise Sources in a Low-Reynolds-number Turbulent Jet at Mach 0.9," *Journal of Fluid Mechanics*, Vol. 438, 2001, pp. 277–305.

[2]Mitchell, B., Lele, S., and Moin, P., "Direct Computation of the Sound Generated by Vortex Pairing in an Axisymmetric Jet," *Journal of Fluid Mechanics*, Vol. 383, 1999, pp. 113–142.

[3]Bogey, C., Bailly, C., and Juvé, D., "Computation of the Sound Radiated by a 3-D Jet Using Large Eddy Simulation," *The 6th AIAA/CEAS Aeroacoustics Conference*, No. 2009 in AIAA 2000, Lahaina, Hawaii, 2000.

[4]Bogey, C., Bailly, C., and Juvé, D., "Noise Investigation of a High Subsonic, Moderate Reynolds Number Jet Using a Compressible Large Eddy Simulation," *Theoret. Comput. Fluid Dynamics*, Vol. 16, No. 4, 2003, pp. 273–297.

[5]Bogey, C. and Bailly, C., "LES of a High Reynolds, High Subsonic Jet : Effects of the Inflow Conditions on Flow and Noise." *The 9th AIAA/CEAS Aeroacoustics Conference*, No. 3170 in AIAA 2003, Hilton Head, South Carolina, 2003.

[6]Bogey, C. and Bailly, C., "Investigation of Subsonic Jet Noise Using LES : Mach and Reynolds Number Effects." *The 10th AIAA/CEAS Aeroacoustics Conference*, No. 3023 in AIAA 2004, Manchester, United Kingdom, 2004.

[7]Mankbadi, R., Shih, S., Hixon, R., and Povinelli, L., "Direct Computation of Jet Noise Produced by Large-Scale Axisymmetric Structures," *J. Propulsion and Power*, Vol. 16, No. 2, 2000, pp. 207–215.

[8]Mankbadi, R., "Review of Computational Aeroacoustics in Propulsion Systems," *J. Propulsion and Power*, Vol. 15, No. 4, 1999, pp. 504–512.

[9]Kirchhoff, G., "Zur Theorie der Lichtstrahlen," *Annalen der Physik und Chemie*, Vol. 18, 1883, pp. 663–695.

[10]Lyrintzis, A., "Review: The Use of Kirchhoff's Method in Computational Aeroacoustics," *ASME: Journal of Fluids Engineering*, Vol. 116, 1994, pp. 665–676.

[11]Freund, J., Lele, S., and Moin, P., "Calculation of the Radiated Sound Field Using an Open Kirchhoff Surface," *AIAA Journal*, Vol. 34, No. 5, 1996, pp. 909–916.

[12]Uzun, A., *3-D Large-Eddy Simulation for Jet Aeroacoustics*, Ph.D. thesis, School of Aeronautics and Astronautics, Purdue University, West Lafayette, IN, 2003.

[13]Uzun, A., Lyrintzis, A., and Blaisdell, G., "Coupling of Integral Acoustic Methods with LES for Jet Noise Prediction," *International Journal of Aeroacoustics*, Vol. 3, No. 4, 2005, pp. 297–346.

[14]Andersson, N., Eriksson, L.-E., and Davidson, L., "Investigation of an Isothermal Mach 0.75 Jet and its Radiated Sound Using Large-Eddy Simulation and Kirchhoff Surface Integration," *International Journal of Heat and Fluid Flow*, Vol. 26, No. 3, 2005, pp. 393–410.

[15]Andersson, N., *A Study of Mach 0.75 Jets and Their Radiated Sound Using Large-Eddy Simulation*, Licentiate thesis, Division of Thermo and Fluid Dynamics, Chalmers University of Technology, Gothenburg, 2003.

[16]Andersson, N., Eriksson, L.-E., and Davidson, L., "Large-Eddy Simulation of Subsonic Turbulent Jets and Their Radiated Sound," *AIAA Journal*, Vol. 43, No. 9, 2005, pp. 1899–1912.

[17]DeBonis, J. and Scott, J., "A Large-Eddy Simulation of a Turbulent Compressible Round Jet," *AIAA Journal*, Vol. 40, No. 7, 2002, pp. 1346–1354.

[18]Morris, P., Scheidegger, T., and Long, L., "Jet Noise Simulations for Circular Nozzles," *The 6th AIAA/CEAS Aeroacoustics Conference*, No. 2009 in AIAA 2000, Lahaina, Hawaii, 2000.

[19]DeBonis, J., "A Large-Eddy Simulation of a High Reynolds Number Mach 0.9 Jet," *The 10th AIAA/CEAS Aeroacoustics Conference*, No. 3025 in AIAA 2004, Manchester, United Kingdom, 2004.

[20]Tucker, P., "Novel MILES computations for jet flows and noise," *International Journal of Heat and Fluid Flow*, Vol. 25, No. 4, 2004, pp. 625–635.

[21]Jordan, P., Gervais, Y., Valiére, J.-C., and Foulon, H., "Final Results from Single Point Measurements," Project deliverable D3.4, JEAN - EU 5th Framework Programme, G4RD-CT-2000-00313, Laboratoire d'Etude Aeródynamiques, Poitiers, 2002.

[22]Jordan, P., Gervais, Y., Valiére, J.-C., and Foulon, H., "Results from Acoustic Field Measurements," Project deliverable D3.6, JEAN - EU 5th Framework Programme, G4RD-CT-2000-00313, Laboratoire d'Etude Aeródynamiques, Poitiers, 2002.

[23]Jordan, P. and Gervais, Y., "Modeling Self and Shear Noise Mechanisms in Anisotropic Turbulence," *The 9th AIAA/CEAS Aeroacoustics Conference*, No. 8743 in AIAA 2003, Hilton Head, South Carolina, 2003.

[24]Power, O., Kerhervé, F., Fitzpatrick, J., and Jordan, P., "Measurements of turbulence statistics in high subsonic jets," *The 10th AIAA/CEAS Aeroacoustics Conference*, No. 3021 in AIAA 2004, Manchester, United Kingdom, 2004.

[25]Billson, M., *Computational techniques for turbulence generated noise*, Ph.D. thesis, Division of Thermo and Fluid Dynamics, Chalmers University of Technology, Gothenburg, 2004.

[26]Erlebacher, G., Hussaini, M., Speziale, C., and Zang, T., "Toward the Large-Eddy Simulation of Compressible Turbulent Flows," *Journal of Fluid Mechanics*, Vol. 238, 1992, pp. 155–185.

[27]Eriksson, L.-E., "Development and Validation of Highly Modular Flow Solver Versions in G2DFLOW and G3DFLOW," Internal report 9970-1162, Volvo Aero Corporation, Sweden, 1995.

[28]Mårtensson, H., Eriksson, L.-E., and Albråten, P., "Numerical simulations of unsteady wakeflow," The 10th ISABE meeting, Nottingham, United Kingdom, 1991.

[29]Wollblad, C., Eriksson, L.-E., and Davidson, L., "Semi-implicit Preconditioning for Wall-bounded Flow," *The 34th AIAA Fluid Dynamics Conference and Exhibit*, No. 2135 in AIAA 2004, Portland, Oregon, 2004.

[30]Billson, M., Eriksson, L.-E., and Davidson, L., "Jet Noise Prediction Using Stochastic Turbulence Modeling," No. 3282 in AIAA 2003, The 9th AIAA/CEAS Aeroacoustics Conference, Hilton Head, South Carolina, 2003.

[31]Billson, M., Eriksson, L.-E., and Davidson, L., "Modeling of Synthetic Anisotropic Turbulence and Its Sound Emission," No. 2857 in AIAA 2004, The 10th AIAA/CEAS Aeroacoustics Conference, Manchester, United Kingdom, 2004.

[32]Billson, M., Eriksson, L.-E., and Davidson, L., "Jet Noise Modeling Using Synthetic Anisotropic Turbulence," No. 3028 in AIAA 2004, The 10th AIAA/CEAS Aeroacoustics Conference, Manchester, United Kingdom, 2004.

[33]Guerts, B., *Elements of Direct and Large-Eddy Simulation*, R.T. Edwards Inc., 2004, ISBN 1-930217-07-2.

[34]Speziale, C., "Galilean Invariance of Subgrid-scale Stress Models in the Large-Eddy Simulation of Turbulence," *Journal of Fluid Mechanics*, Vol. 156, 1985, pp. 55–62.

[35]Sagaut, P., *Large Eddy Simulation for Incompressible Flows; an Introduction*, Scientific Computation, Springer Verlag, 2nd ed., 2002, ISBN 3-540-43753-3.

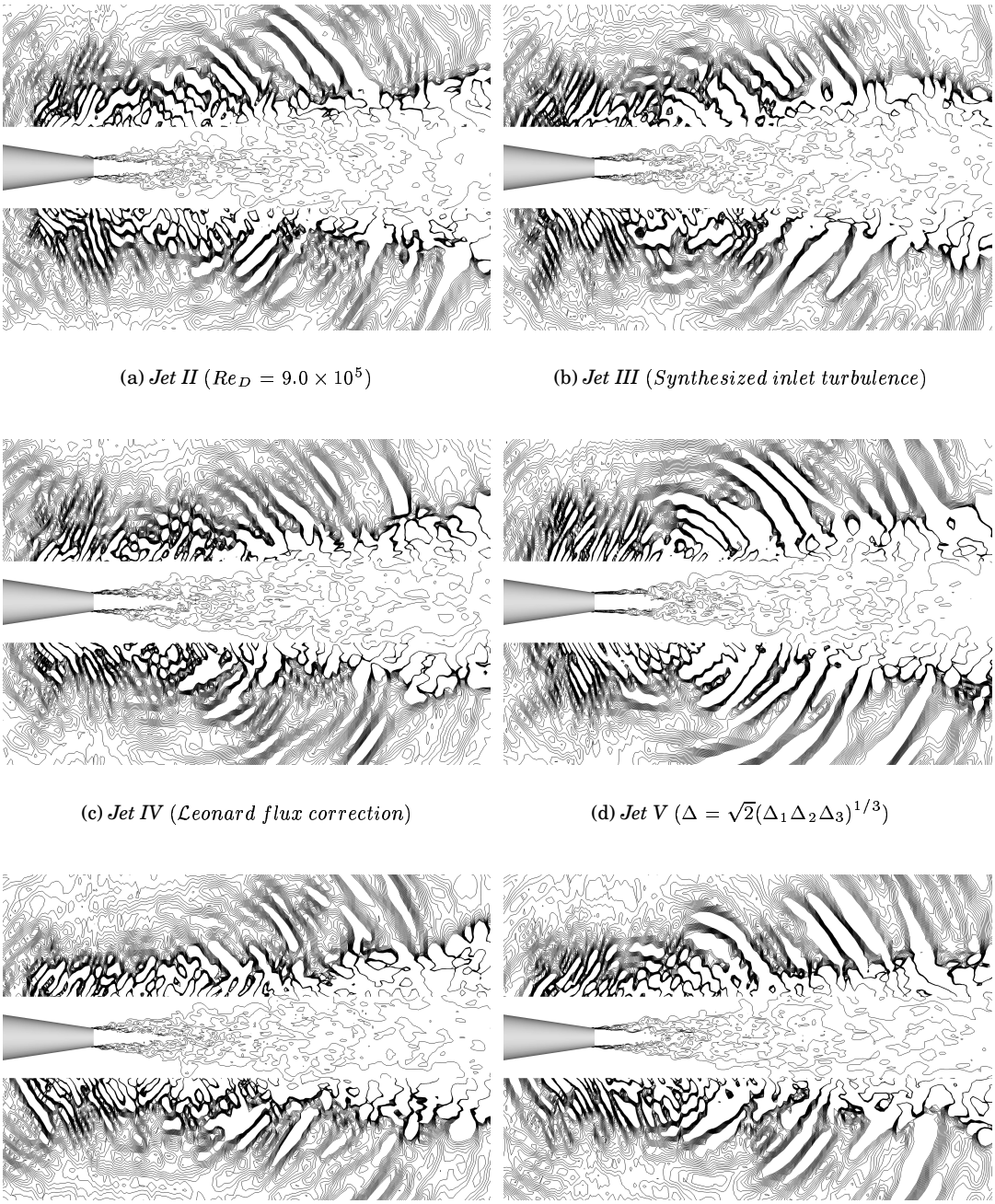

(a) *Jet II* ($Re_D = 9.0 \times 10^5$)

(b) *Jet III* ($Synthesized\ inlet\ turbulence$)

(c) *Jet IV* ($Leonard\ flux\ correction$)

(d) *Jet V* ($\Delta = \sqrt{2}(\Delta_1\Delta_2\Delta_3)^{1/3}$)

(e) *Jet VI* ($\Delta = \min(\Delta_1, \Delta_2, \Delta_3)$)

(f) *Jet VII* ($P_0 = P_0(r)$)

Figure 14. Instantaneous contours of dilatation and entropy for *Jet II – Jet VII*

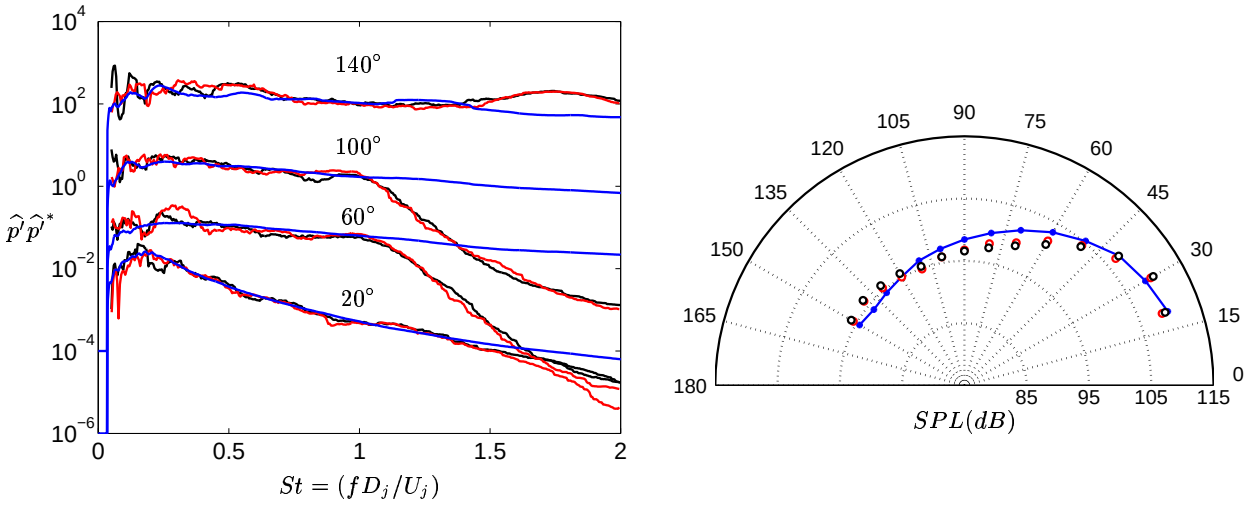

(a) Power spectra (*Jet II*)

(b) Sound pressure levels (*Jet II*)

Figure 15. Power spectra and far-field sound pressure levels for *Jet II* ($Re_D = 9.0 \times 10^5$). The spectra have been staggered by multiplying the amplitude by a factor 10^{2n}, where $n = \left(\frac{\theta - 20}{40}\right)$, θ being the angle from the jet axis. $\widehat{p'}$ denotes the Fourier transform of the pressure fluctuation and $\widehat{p'}^*$ its conjugate. Blue lines and circles denote measured data, red lines and circles correspond to the reference case *Jet I* and black lines and circles denote the predictions for *Jet II*.

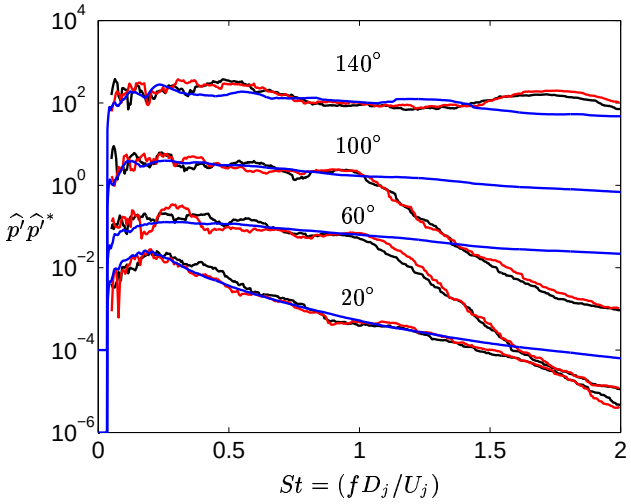

(a) Power spectra (*Jet III*)

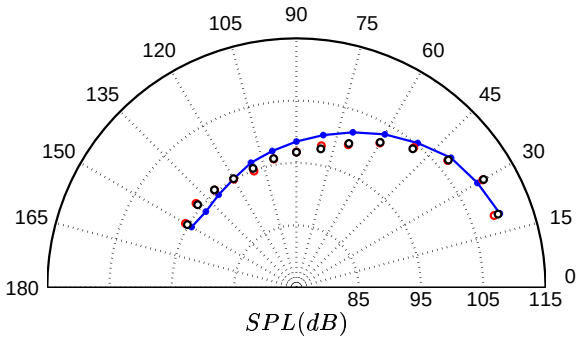

(b) Sound pressure levels (*Jet III*)

Figure 16. Power spectra and far-field sound pressure levels for *Jet III* ($Synthesized\ inlet\ turbulence$)**. For legend see Figure (15).**

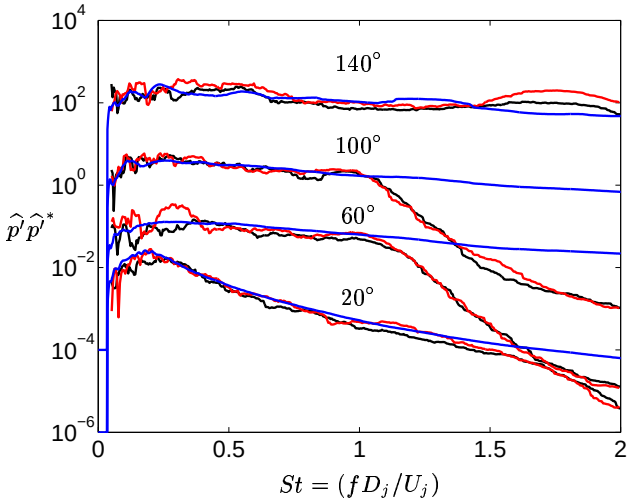

(a) Power spectra (*Jet IV*)

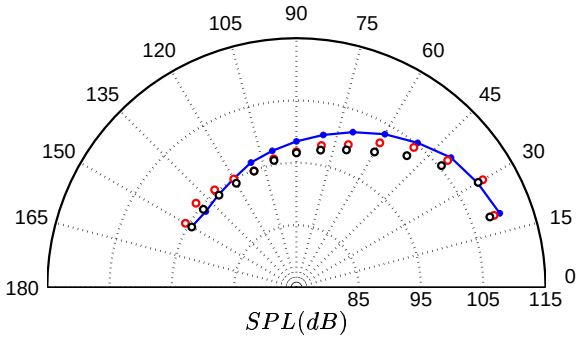

(b) Sound pressure levels (*Jet IV*)

Figure 17. Power spectra and far-field sound pressure levels for *Jet IV* ($Leonard\ flux\ correction$)**. For legend see Figure (15).**

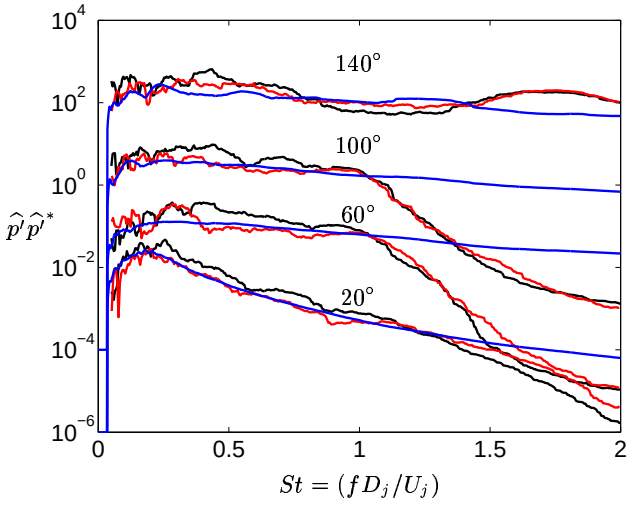

(a) Power spectra (*Jet V*)

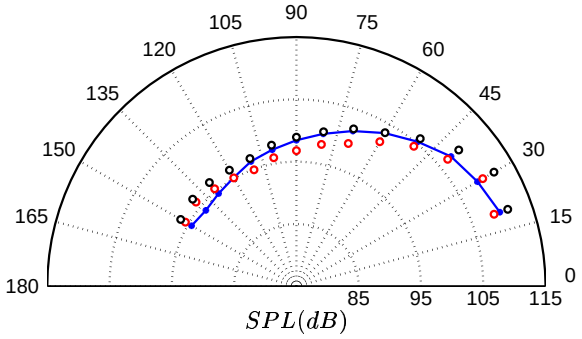

(b) Sound pressure levels (*Jet V*)

Figure 18. Power spectra and far-field sound pressure levels for *Jet V* ($\Delta = \sqrt{2}(\Delta_1\Delta_2\Delta_3)^{1/3}$)**. For legend see Figure (15).**

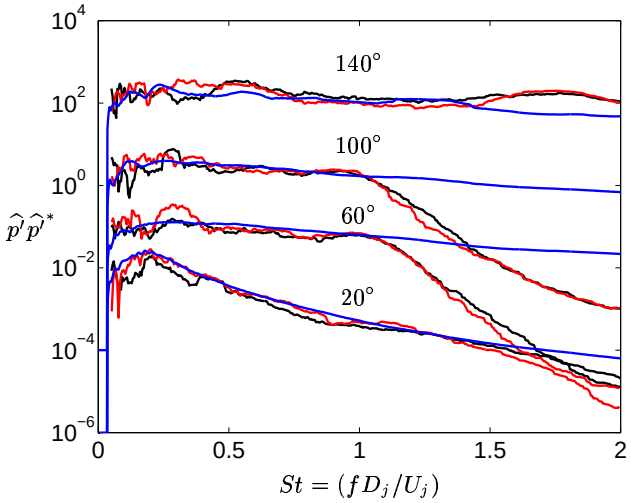

(a) Power spectra (*Jet VI*)

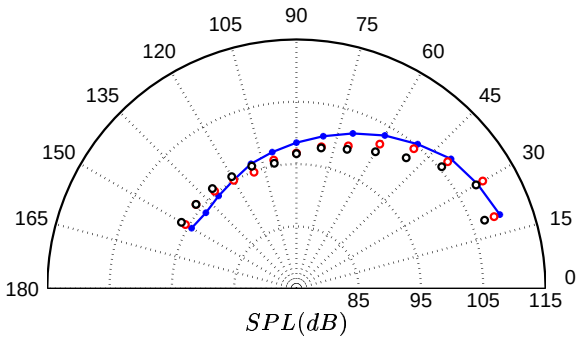

(b) Sound pressure levels (*Jet VI*)

Figure 19. Power spectra and far-field sound pressure levels for *Jet VI* ($\Delta = \min(\Delta_1, \Delta_2, \Delta_3)$)**. For legend see Figure (15).**

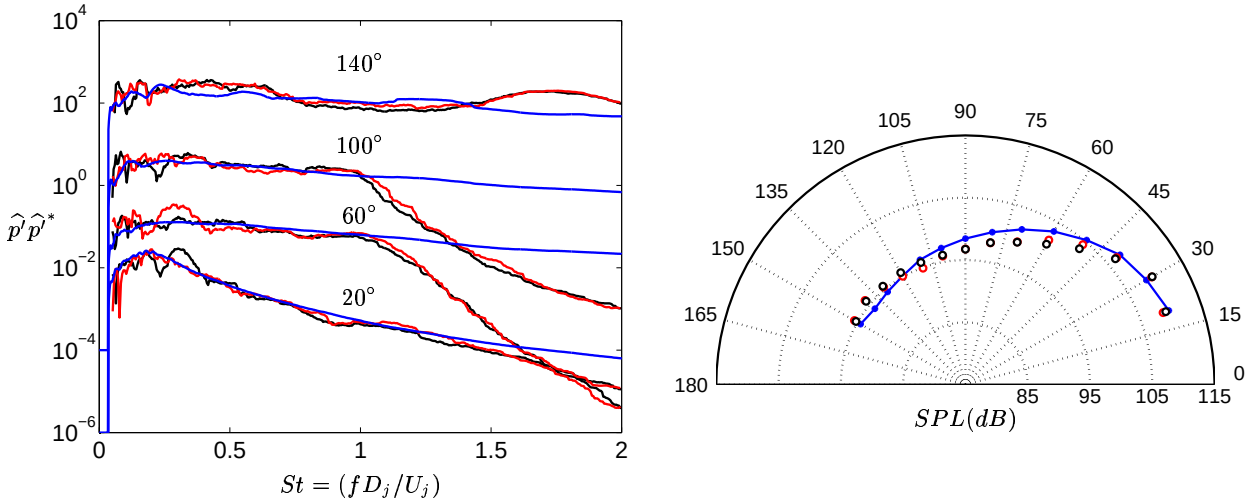

(a) Power spectra (*Jet VII*)

(b) Sound pressure levels (*Jet VII*)

Figure 20. Power spectra and far-field sound pressure levels for *Jet VII* ($P_0 = P_0(r)$). For legend see Figure (15).